mixture containing 0.05 μM sense primer, 0.5 μM antisense primer, 0.2 μM anchor probe, 0.2 μM sensor probe, 10 ng of genomic DNA, and 1 μL of 5X LightCycler 480 genotyping master solution (modified *Taq* DNA polymerase, reaction buffer, dNTP mix, and 15 mM magnesium chloride) in a total volume of 5 μL. The reaction parameters consisted of a 10-minute initial denaturation at 95°C followed by 45 cycles of denaturation at 95°C for 15 seconds, annealing at 55°C for 15 seconds, and extension at 72°C for 15 seconds. After PCR amplification, a melting curve analysis was performed by the reaction's being held at 95°C for 1 minute and at 40°C for 1 minute and then slowly heated to 85°C with a ramp rate of 2°C per second. The melting curve data were collected and classified using the LightCycler genotyping software.

Statistical analysis

The allele frequency was calculated, and the deviation of the genotype distribution from Hardy-Weinberg equilibrium was determined using a chi-square test. Analysis of variance with or without adjustment (age and height) was used to compare the mean values of basic and clinical characteristics and energy intake levels among genotype groups. The odds ratio and 95% confidence interval for the prevalence of MetS between different genotype groups was evaluated using a multiple logistic regression model with or without adjustment for age and height. Furthermore, the correlations between HbA1c level (a continuous variable) and *CDKAL1* genotype among the energy intake groups, or the energy intake levels among the genotype groups, were examined by multiple linear regression analyses, which were also adjusted for age, height, or current smoking and alcohol drinking status. Seven subjects were excluded because of antidiabetes treatment. Analysis of covariance was used to examine the gene-environment interaction effects on HbA1c and fasting blood glucose level. SPSS for Windows, version 11.0 (SPSS Inc., Chicago, Illinois), was used for all analyses. A P value less than 0.05 was considered significant. The corrected significance threshold level using the Bonferroni method, based on these 2 interaction tests, was $P = 0.05/2 = 0.025$). Although we analyzed the gene-environment interaction effect on the blood glucose level, we discuss the effect related to HbA1c rather than to fasting blood glucose.

RESULTS

The frequency of the minor allele, C, was 0.492, which was similar to the frequency in the Japanese general population (0.456; http://www.hapmap.org/). The frequencies of the CC, CT, and TT genotypes of rs9465871 among the 313 Japanese men were 25.2%, 47.9%, and 26.8%, respectively. The genotype distribution did not deviate from Hardy-Weinberg equilibrium ($P = 0.46$).

Subjects were characterized according to age, height, body weight, body mass index, waist circumference, blood pressure, serum lipid level, fasting plasma glucose concentration, and HbA1c level and were categorized into 3 groups based on their genotype: CC, CT, and TT. There was no significant linear trend for the mean age- and height-adjusted differences in age, body weight, body mass index, waist circumference, systolic blood pressure, diastolic blood pressure, serum lipids, fasting plasma glucose, HbA1c, or age-adjusted height among the 3 *CDKAL1* genotype groups (data not shown). The adjusted mean HbA1c level in the CC genotype group (5.2% (SD, 1.2)) was higher than that in the CT group (5.0% (SD, 0.85); $P = 0.10$) or the TT group (4.99% (SD, 0.60)), but the difference was not significant ($P = 0.07$). Thus, we further classified the participants into 2 groups: TT + CT and CC, which was the homozygous recessive genotype associated with type 2 diabetes (9) and impaired fasting glucose in the previous replication study (24). We found no significant differences in age, height, body weight, body mass index, waist circumference, systolic blood pressure, diastolic blood pressure, serum lipid, or fasting plasma glucose levels between the TT + CT and CC genotype groups, even after adjustment for relevant confounding variables (Table 1). In addition, we found no significant differences for the lifestyle factors of dietary energy intake and current smoking and alcohol drinking status when comparing the TT + CT and CC genotype groups (Table 1). However, HbA1c levels were significantly higher in the CC group than in the TT + CT group ($P = 0.04$). Even after we excluded the 7 subjects with diabetes, carriers of the CC genotype had a significantly higher mean HbA1c level than persons with the TT + CT genotype ($P = 0.039$, linear regression) after adjustment for age, height, current smoking and drinking status, and energy intake.

The prevalence of MetS was also significantly different between the 2 *CDKAL1* genotype groups, with a prevalence of 25.6% in the CC group and 16.3% in the TT + CT group. After adjustment for age and height, the odds ratio for the CC group as compared with the TT + CT group was 2.18 (95% confidence interval: 1.06, 4.48) ($P = 0.035$).

We examined not only HbA1c but also fasting glucose concentration according to *CDKAL1* genotype. We did not find a significant relation between fasting glucose level and the *CDKAL1* variants (data not shown).

When analyzing the HbA1c levels of the CC and TT + CT groups after adjusting for age, height, and current smoking and drinking status and after grouping the subjects according to their dietary energy intake, we found the HbA1c level of the CC group with the highest energy intake to be significantly higher than that of the TT + CT group (5.6% (SD, 1.7) vs. 5.0% (SD, 0.5), $P = 0.025$; Figure 1). No such difference in HbA1c levels was found in the low-energy-intake group (CC vs. TT + CT: 4.9% (SD, 0.7) vs. 5.1% (SD, 1.1), $P = 0.99$; Figure 1) or the middle-energy-intake group (CC vs. TT + CT: 5.2% (SD, 0.9) vs. 4.9% (SD, 0.4), $P = 0.37$; Figure 1). Furthermore, the HbA1c level was also significantly different after accounting for the interaction between energy intake as a categorical variable and *CDKAL1* genotype ($P = 0.028$) and after adjusting for age, height, and current smoking and drinking status. The significant interaction effect ($P = 0.028$) was marginally greater than the conservative, Bonferroni-corrected effect ($P = 0.025$).

We also examined the correlation between HbA1c levels and energy intake in subjects with the CC and TT + CT genotypes. The TT + CT group did not show significant

Table 1. Characteristics of Subjects According to Cyclin-Dependent Kinase 5 Regulatory Subunit-Associated Protein 1-Like 1 (*CDKAL1*) Genotype, Japan, 2003

	Genotype				*P* Value[a]
	CC (n = 79)		TT + CT (n = 234)		
	Mean (SD)	%	Mean (SD)	%	
Age, years	45.5 (11.7)		45.8 (11.7)		0.82
Height, cm	168.1 (6.8)		168.9 (6.1)		0.29
Body weight, kg	66.0 (10.3)		66.8 (11.5)		0.55
Body mass index[b]	23.4 (3.4)		23.4 (3.6)		0.90
Waist circumference, cm	83.6 (9.6)		83.9 (9.7)		0.75
Serum total cholesterol, mg/dL	208.6 (41.6)		206.3 (35.6)		0.68
Serum triglycerides, mg/dL	137.8 (87.5)		131.6 (81.9)		0.27
Serum high density lipoprotein cholesterol, mg/dL	52.9 (13.1)		56.2 (14.3)		0.07
Fasting plasma glucose, mg/dL	101.3 (34.6)		100.4 (33.4)		0.68
Serum hemoglobin A1c, %	5.2 (1.2)		5.0 (0.8)		0.04*
Systolic blood pressure, mm Hg	132.2 (18.8)		135.2 (17.5)		0.21
Diastolic blood pressure, mm Hg	79.5 (13.5)		82.4 (12.2)		0.09
Energy intake, kJ/day	7,700.8 (1,886.1)		7,724.0 (2,064.1)		0.76
Current smoking		57.5		60.8	0.62
Current alcohol consumption		69.9		74.5	0.44
Family history of diabetes		17.9		14.1	0.46
Prevalence of metabolic syndrome		25.6		16.3	0.035*

Abbreviations: ANOVA, analysis of variance; SD, standard deviation.

* $P < 0.05$.

[a] P values were derived using an additive model and were determined by unadjusted ANOVA (age), ANOVA adjusted for age (height), ANOVA adjusted for age and height (other continuous traits), or chi-square test (categorized traits).

[b] Weight (kg)/height $(m)^2$.

positive correlations between HbA1c and energy intake, but the CC group did show a correlation (Figure 2). In the TT + CT group, the regression coefficient was 0.16, and P equaled 0.012 for the trend after adjustment for age, height, and smoking and drinking status (Figure 2A). In the CC group, the regression coefficient was 0.25 and P was 0.037 for the trend (Figure 2B). Furthermore, when we examined the interaction term for *CDKAL1* genotype and energy intake using the multivariate-adjusted general linear model and adjusted for age, height, and current smoking and drinking status, the positive correlation between HbA1c and energy intake was significantly greater in the CC genotype group than in the TT + CT genotype group ($P < 0.001$; Figure 2C). These results indicate that HbA1c levels tend to be higher in subjects with the CC genotype than in those with the TT + CT genotype when energy intake is higher.

DISCUSSION

The present study showed that a polymorphism in the type 2 diabetes risk-conferring *CDKAL1* gene is associated with elevated HbA1c levels and an increased prevalence of MetS in apparently healthy Japanese men. The risk allele and genetic models were the same as in the previous study of type 2 diabetes (9).

HbA1c is a minor component of hemoglobin, and the proportion of HbA1c in total hemoglobin (%) is considered to be an integrated measure of blood glucose concentrations for 6–8 weeks prior to HbA1c measurement (25). Therefore, HbA1c is widely accepted as a standard method for determining long-term glycemic control in diabetic patients (26). HbA1c has also been suggested to serve as a predictor of progression to type 2 diabetes in nondiabetic persons (27, 28), as well as for MetS (29). Sung et al. (29) reported that an HbA1c level of 5.5% represents the value with maximum sensitivity and specificity for the diagnosis of MetS in a large-scale cross-sectional study among nondiabetic South Korean adults. In addition, an HbA1c level of 5.2% or less has been recommended in recent guidelines from the Japanese Ministry of Health, Labour, and Welfare (30) to aid in the diagnosis of MetS. Therefore, although the current effect of *CDKAL1* variants on HbA1c levels is within the normal range and is modest (CC vs. TT + CT: 5.2% (SD, 1.2) vs. 5.0% (SD, 0.8)), we think that this difference is an indication of a subtle dysglycemic phenotype detected prior to the elevation in

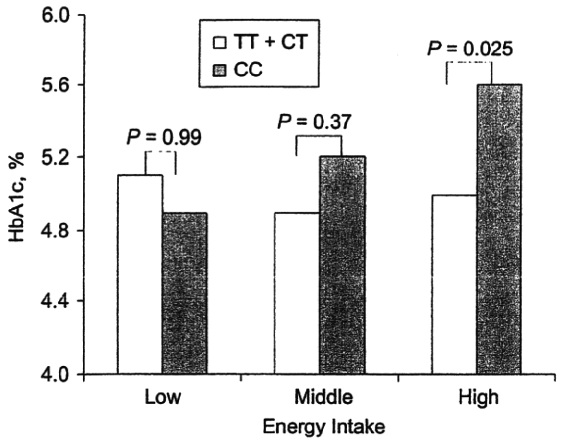

Figure 1. Mean hemoglobin A_{1c} (HbA1c) level according to cyclin-dependent kinase 5 regulatory subunit-associated protein 1-like 1 (*CDKAL1*) genotype, Japan, 2003. Subjects were further grouped by tertile of energy intake (low (2,474.5–6,788.6 kJ/day), middle (6,790.3–8,465.6 kJ/day), or high (8,499.9–17,740.0 kJ/day)), with adjustment for age, height, and current smoking and alcohol drinking status. The HbA1c level of the CC group with the highest energy intake was significantly higher than that of the TT + CT group.

fasting plasma glucose. In this regard, notably, normal HbA1c is associated with markers of inflammation in patients with coronary artery disease (31).

Our results, obtained from a cohort of male workers, corroborate previous reports in which *CDKAL1* genotype was associated with altered insulin responsiveness (10, 14, 15) or the first phase of insulin secretion in normal subjects (32). Moreover, we showed that the *CDKAL1* variant rs9465871 affects HbA1c levels in a manner dependent on increased energy intake, implying that the effect of rs9465871 on glycemic control is influenced by nutritional factors. The association of the *CDKAL1* variant with MetS poses an intriguing question regarding the mechanism of the development and progression of the disease. To the best of our knowledge, this is the first study to have found an interaction effect of the type 2 diabetes genetic marker *CDKAL1* and a lifestyle-related factor, specifically energy intake, on MetS in a healthy Japanese population.

MetS is comprised of 4 typical components: abdominal obesity, hypertension, dyslipidemia, and impaired fasting glucose concentration. Insulin resistance is thought to play a primary role in the pathophysiology of MetS; in the natural course of the disease, insulin resistance is initially counterbalanced by a compensatory increase in insulin secretion to maintain normal glucose tolerance. However, the increase in insulin secretion is eventually unable to offset the severe degree of insulin resistance, and overt type 2 diabetes develops. Our results suggest that β-cell dysfunction might be involved from the early stages of MetS, and it is tempting to speculate that the dysglycemic component of MetS might already be influenced by impaired insulin secretion. We conclude that *CDKAL1*, which is known to play a role in insulin secretion and type 2 diabetes, interacts with energy intake and confers a risk for the dysglycemic phenotype of MetS.

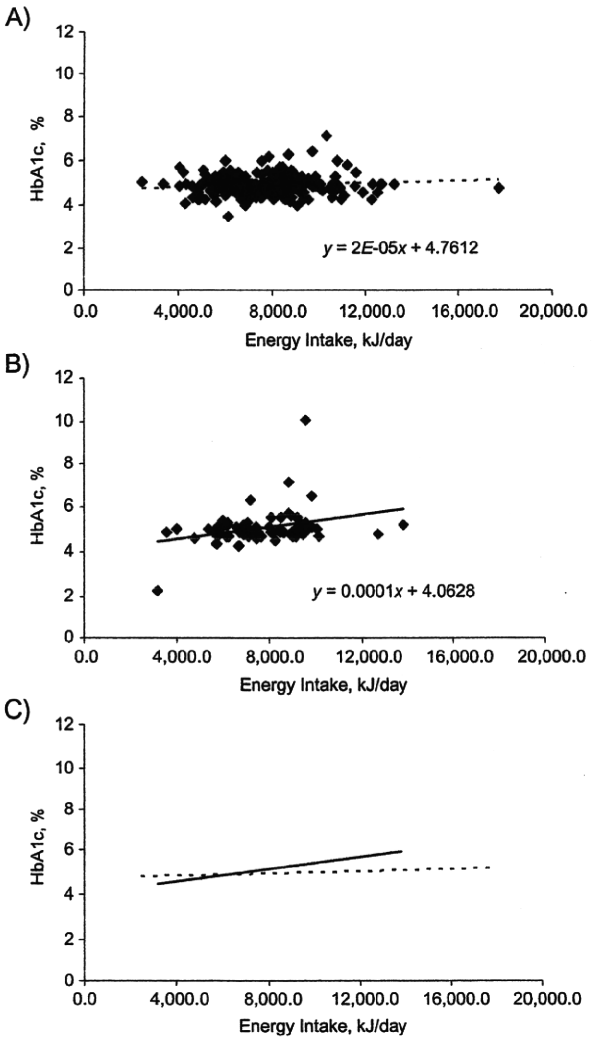

Figure 2. Effects of daily energy intake on hemoglobin A_{1c} (HbA1c) level in subjects with different cyclin-dependent kinase 5 regulatory subunit-associated protein 1-like 1 (*CDKAL1*) genotypes, Japan, 2003. Results were adjusted for age, height, and current smoking and alcohol drinking status. The regression lines are indicated in each section: A) TT + CT genotype group (*P* for slope = 0.012); B) CC genotype group (*P* for slope = 0.037); C) both genotype groups (solid line, CC; dotted line, TT + CT). The *P* value for interaction was less than 0.001.

Our study had the following limitations. First, dietary energy intake was self-reported, derived from answers to a validated semiquantitative food frequency questionnaire, which might have introduced measurement bias. Second, the study sample size within this cohort was not large enough to detect a gene-nutrient interaction effect, because the statistical power was low. We speculate that the subjects' unique ethnicity may have been the reason why we detected an interaction. In addition, in a previous study, Jakes et al. (33) reported that energy intake was related to

body size, which is correlated with the energy expenditure of physical activity. In our study, we adjusted for body size as a confounding variable; however, there may have been other residual confounding factors not accounted for in our analyses.

The overlap of this genetic risk factor with impaired insulin secretion in patients with type 2 diabetes and MetS suggests a commonality in their etiology. This issue needs to be considered by taking into account ethnic differences, because β-cell function has been shown to be lower in Japanese-American and Chinese-American populations than in African-American and non-Hispanic white populations (34).

Furthermore, Moore et al. (35) reported on the effect of the diabetes gene on lifestyle interventions among nondiabetic high-risk participants in the Diabetes Prevention Program and found no evidence of interactions between *CDKAL1* and lifestyle (or metformin). Thus, the *CDKAL1* polymorphism may potentially play a role in the initial phase of dysglycemia. Our findings suggest that *CDKAL1* may not only be a good genetic marker for the detection of MetS, even in a healthy population, but also may provide descriptive information about lifestyle modification in the prevention of MetS. However, additional studies are warranted for further exploration of the interaction effect, as well as to determine when and how insulin secretion affects the pathogenesis of MetS.

ACKNOWLEDGMENTS

Author affiliations: Department of Neurology, School of Medicine, Keio University, Tokyo, Japan (Koichi Miyaki, Htay Lwin, Yutaka Tomita, Haruhiko Hoshino, Norihiro Suzuki); and Department of Molecular Epidemiology, Medical Research Institute, Tokyo Medical and Dental University, Tokyo, Japan (Koichi Miyaki, Than Oo, Yixuan Song, Htay Lwin, Masaaki Muramatsu).

This study was supported by the Japanese Ministry of Education, Science, Sports, and Culture (Grant-in-Aid for Scientific Research 19590581).

Conflict of interest: none declared.

REFERENCES

1. Eckel RH, Grundy SM, Zimmet PZ. The metabolic syndrome. *Lancet*. 2005;365(9468):1415–1428.
2. Ford ES, Giles WH, Dietz WH. Prevalence of the metabolic syndrome among US adults: findings from the Third National Health and Nutrition Examination Survey. *JAMA*. 2002; 287(3):356–359.
3. Miyatake N, Kawasaki Y, Nishikawa H, et al. Prevalence of metabolic syndrome in Okayama prefecture, Japan. *Intern Med*. 2006;45(2):107–108.
4. Grundy SM, Brewer HB Jr, Cleeman JI, et al. Definition of metabolic syndrome: report of the National Heart, Lung, and Blood Institute/American Heart Association conference on scientific issues related to definition. *Circulation*. 2004;109(3): 433–438.
5. Moller DE, Kaufman KD. Metabolic syndrome: a clinical and molecular perspective. *Annu Rev Med*. 2005;56:45–62.
6. Roche HM, Phillips C, Gibney MJ. The metabolic syndrome: the crossroads of diet and genetics. *Proc Nutr Soc*. 2005;64(3): 371–377.
7. Song Y, Miyaki K, Araki J, et al. The interaction between the interleukin 6 receptor gene genotype and dietary energy intake on abdominal obesity in Japanese men. *Metabolism*. 2007; 56(7):925–930.
8. Zhang L, Miyaki K, Nakayama T, et al. Cell death-inducing DNA fragmentation factor alpha-like effector A (CIDEA) gene V115F (G→T) polymorphism is associated with phenotypes of metabolic syndrome in Japanese men. *Metabolism*. 2008;57(4):502–505.
9. Wellcome Trust Case-Control Consortium. Genome-wide association study of 14,000 cases of seven common diseases and 3,000 shared controls. *Nature*. 2007;447(7145):661–678.
10. Steinthorsdottir V, Thorleifsson G, Reynisdottir I, et al. A variant in CDKAL1 influences insulin response and risk of type 2 diabetes. *Nat Genet*. 2007;39(6):770–775.
11. Zeggini E, Weedon MN, Lindgren CM, et al. Replication of genome-wide association signals in UK samples reveals risk loci for type 2 diabetes. *Science*. 2007;316(5829): 1336–1341.
12. Omori S, Tanaka Y, Takahashi A, et al. Association of CDKAL1, IGF2BP2, CDKN2A/B, HHEX, SLC30A8, and KCNJ11 with susceptibility to type 2 diabetes in a Japanese population. *Diabetes*. 2008;57(3):791–795.
13. Takeuchi F, Serizawa M, Yamamoto K, et al. Confirmation of multiple risk loci and genetic impacts by a genome-wide association study of type 2 diabetes in the Japanese population. *Diabetes*. 2009;58(7):1690–1699.
14. Palmer ND, Goodarzi MO, Langefeld CD, et al. Quantitative trait analysis of type 2 diabetes susceptibility loci identified from whole genome association studies in the Insulin Resistance Atherosclerosis Family Study. *Diabetes*. 2008;57(4): 1093–1100.
15. Stancáková A, Pihlajamäki J, Kuusisto J, et al. Single-nucleotide polymorphism rs7754840 of CDKAL1 is associated with impaired insulin secretion in nondiabetic offspring of type 2 diabetic subjects and in a large sample of men with normal glucose tolerance. EUGENE2 Consortium. *J Clin Endocrinol Metab*. 2008;93(5):1924–1930.
16. Ng MC, Park KS, Oh B, et al. Implication of genetic variants near TCF7L2, SLC30A8, HHEX, CDKAL1, CDKN2A/B, IGF2BP2, and FTO in type 2 diabetes and obesity in 6,719 Asians. *Diabetes*. 2008;57(8):2226–2233.
17. Kim WY, Kim JE, Choi YJ, et al. Nutritional risk and metabolic syndrome in Korean type 2 diabetes mellitus. *Asia Pac J Clin Nutr*. 2008;17(suppl 1):47–51.
18. Kim HS, Park SY, Grandinetti A, et al. Major dietary patterns, ethnicity, and prevalence of type 2 diabetes in rural Hawaii. *Nutrition*. 2008;24(11-12):1065–1072.
19. Wei FY, Nagashima K, Ohshima T, et al. Cdk5-dependent regulation of glucose-stimulated insulin secretion [letter]. *Nat Med*. 2005;11(10):1104–1108.
20. Ubeda M, Rukstalis JM, Habener JF. Inhibition of cyclin-dependent kinase 5 activity protects pancreatic beta cells from glucotoxicity. *J Biol Chem*. 2006;281(39): 28858–28864.
21. Arai H, Yamamoto A, Matsuzawa Y, et al. Prevalence of metabolic syndrome in the general Japanese population in 2000. *J Atheroscler Thromb*. 2006;13(4):202–208.

22. Takahashi K, Yoshimura Y, Kaimoto T, et al. Validation of a food frequency questionnaire based on food groups for estimating individual nutrient intake [in Japanese]. *Jpn J Nutr.* 2001;59(5):221–232.
23. Miyaki K, Sutani S, Kikuchi H, et al. Increased risk of obesity resulting from the interaction between high energy intake and the Trp64Arg polymorphism of the β3-adrenergic receptor gene in healthy Japanese men. *J Epidemiol.* 2005;15(6): 203–210.
24. Wu Y, Li H, Loos RJ, et al. Common variants in CDKAL1, CDKN2A/B, IGF2BP2, SLC30A8, and HHEX/IDE genes are associated with type 2 diabetes and impaired fasting glucose in a Chinese Han population. *Diabetes.* 2008;57(10):2834–2842.
25. Bunn HF. Evaluation of glycosylated hemoglobin diabetic patients. *Diabetes.* 1981;30(7):613–617.
26. Larsen ML, Hørder M, Mogensen EF. Effect of long-term monitoring of glycosylated hemoglobin levels in insulin-dependent diabetes mellitus. *N Engl J Med.* 1990;323(15): 1021–1025.
27. Rohlfing CL, Little RR, Wiedmeyer HM, et al. Use of GHb (HbA1c) in screening for undiagnosed diabetes in the U.S. population. *Diabetes Care.* 2000;23(2):187–191.
28. Droumaguet C, Balkau B, Simon D, et al. Use of HbA_{1c} in predicting progression to diabetes in French men and women: Data from an Epidemiological Study on the Insulin Resistance Syndrome (DESIR). *Diabetes Care.* 2006;29(7): 1619–1625.
29. Sung KC, Rhee EJ. Glycated haemoglobin as a predictor for metabolic syndrome in non-diabetic Korean adults. *Diabet Med.* 2007;24(8):848–854.
30. Masuzoe Y. Notification on the criteria for health checkup and health guidance [in Japanese]. Tokyo, Japan: Ministry of Health, Labour and Welfare; 2008. (http://www.mhlw.go.jp/bunya/shakaihosho/iryouseido01/dl/info03i-2.pdf). (Accessed May 1, 2009).
31. Gustavsson CG, Agardh CD. Markers of inflammation in patients with coronary artery disease are also associated with glycosylated haemoglobin A1c within the normal range. Eur Heart J. 2004;25(23):2120–2124.
32. Groenewoud MJ, Dekker JM, Fritsche A, et al. Variants of CDKAL1 and IGF2BP2 affect first-phase insulin secretion during hyperglycaemic clamps. *Diabetologia.* 2008;51(9): 1659–1663.
33. Jakes RW, Day NE, Luben R, et al. Adjusting for energy intake—what measure to use in nutritional epidemiological studies? *Int J Epidemiol.* 2004;33(6):1382–1386.
34. Torréns JI, Skurnick J, Davidow AL, et al. Ethnic differences in insulin sensitivity and beta-cell function in premenopausal or early perimenopausal women without diabetes: the Study of Women's Health Across the Nation (SWAN). *Diabetes Care.* 2004;27(2):354–361.
35. Moore AF, Jablonski KA, McAteer JB, et al. Extension of type 2 diabetes genome-wide association scan results in the Diabetes Prevention Program. *Diabetes.* 2008;57(9):2503–2510.

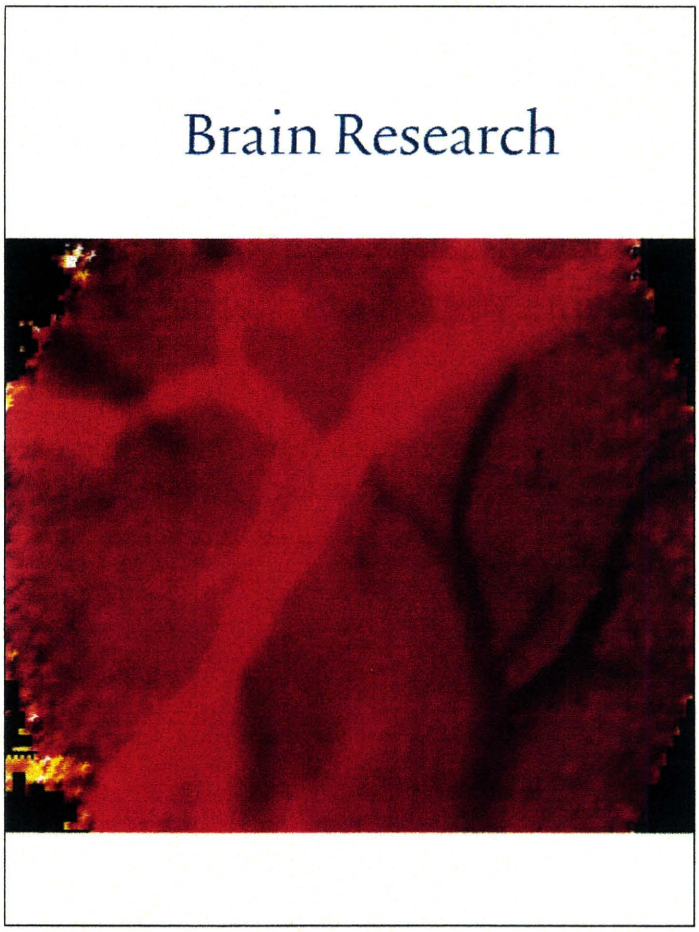

BRAIN RESEARCH 1372 (2011) 59–69

available at www.sciencedirect.com

ScienceDirect

www.elsevier.com/locate/brainres

BRAIN RESEARCH

Research Report

Long-term, repeated measurements of mouse cortical microflow at the same region of interest with high spatial resolution

Yutaka Tomita[a,b,c,*], *Elisabeth Pinard*[a], *Alexy Tran-Dinh*[a], *Istvan Schiszler*[b], *Nathalie Kubis*[a], *Minoru Tomita*[b], *Norihiro Suzuki*[b], *Jacques Seylaz*[a]

[a]*Cardiovascular Research Center Lariboisière, INSERM U 689, Université Paris 7, Paris, France*
[b]*Department of Neurology, Keio University School of Medicine, Shinanomachi, Shinjuku-ku, Tokyo, Japan*
[c]*Tomita Hospital, Motojuku-cho, Okazaki, Aichi, Japan*

ARTICLE INFO

Article history:
Accepted 5 November 2010
Available online 25 November 2010

Keywords:
2-D flow map
Confocal microscopy
Focal cerebral ischemia
Mouse
Cerebral blood flow
Optical imaging

ABSTRACT

A method for long-term, repeated, semi-quantitative measurements of cerebral microflow at the same region of interest (ROI) with high spatial resolution was developed and applied to mice subjected to focal arterial occlusion. A closed cranial window was chronically implanted over the left parieto-occipital cortex. The anesthetized mouse was placed several times, e.g., weekly, under a dynamic confocal microscope, and Rhodamine B-isothiocyanate-dextran was each time intravenously injected as a bolus, while microflow images were video recorded. Left and right tail veins were sequentially catheterized in a mouse three times at maximum over a 1.5 months' observation period. Smearing of the input function resulting from the use of intravenous injection was shown to be sufficiently small. The distal middle cerebral artery (MCA) was thermocoagulated through the cranial window in six mice, and five sham-operated mice were studied in parallel. Dye injection and video recording were conducted four times in this series, i.e., before and at 10 min, 7 and 30 days after sham operation or MCA occlusion. Pixelar microflow values (1/MTT) in a matrix of approximately 50×50 pixels were displayed on a two-dimensional (2-D) map, and the frequency distribution of the flow values was also calculated. No significant changes in microflow values over time were detected in sham-operated mice, while the time course of flow changes in the ischemic penumbral area in operated mice was similar to those reported in the literature. This method provides a powerful tool to investigate long-term changes in mouse cortical microflow under physiological and pathological conditions.

1. Introduction

The heterogeneity of brain tissue and vascularization makes difficult to follow the spatial and temporal evolution of cerebral blood flow (CBF). Presently, CBF spatial heterogeneity is best evaluated using autoradiographic techniques, but this can be done only at a single time point, because the animal must be sacrificed. The microsphere method offers the

* *Corresponding author.* Department of Neurology, Keio University School of Medicine, Shinanomachi, Shinjuku-ku, Tokyo, Japan. Fax: +81 3 3353 1272.
E-mail address: yutakacnrs@aol.com (Y. Tomita).

0006-8993/$ – see front matter © 2010 Elsevier B.V. All rights reserved.
doi:10.1016/j.brainres.2010.11.014

advantage of repeated measurements, but also requires post-mortem analysis. Laser Doppler flowmetry (LDF) is a reliable method for estimation of relative changes of CBF but has poor spatial resolution. The latest development, laser speckle flowmetry (Ayata et al., 2004), represents a significant improvement in terms of temporal and spatial resolution, but its value as a quantitative method remains open to question (Duncan and Kirkpatrick, 2008).

The optical method developed and validated by Schiszler et al. (2000) makes it possible to visualize microflow in the cerebral cortex of rats with a high spatial resolution of 40 μm/pixel. It is based upon a photoelectric method originally developed by Tomita et al. (1978), using transillumination of the cat cerebral cortex by a small tungsten lamp and a photosensor system for recording of the light transparency changes, after the intracarotid injection of a bolus of carbon black. There is no doubt as to its reliability, since dye transit with flow through the tissue is directly observed. The modifications reported by Schiszler et al. (2000) were that saline was used as a negative indicator of blood, the region of interest (ROI) was transilluminated by optical fiber-conducted light from a halogen source, and pixelar microflow was calculated in a matrix of 50×50 pixels with KEIO-IS1 (Matlab domain software). The mean transit time (MTT) of saline is calculated in each pixel, providing a two-dimensional (2-D) map of the microregional flow distribution. This method was applied to rats to study ischemia-induced (Tomita et al., 2002) and cortical spreading depression-induced (Tomita et al., 2005a) changes in cortical microflow. Its main disadvantage is invasiveness, because it requires the insertion of a glass fiber into brain tissue. However, its main advantage lies in its ability to produce 2-D flow maps in a small area with a high spatial resolution of 40 μm/pixel.

In parallel, Seylaz et al. (1999) developed a method to continuously visualize microvascular blood flow through a closed cranial window in rats, using laser scanning dynamic confocal microscopy. This method combines the approaches of Hudetz et al. (1992) and Dirnagl et al. (1991) in order to video monitor fluorescent erythrocytes and dextran flowing through microvessels. This dynamic method was also applied to mice (Tomita et al., 2005b) with the additional advantage of repetitive long-term measurements.

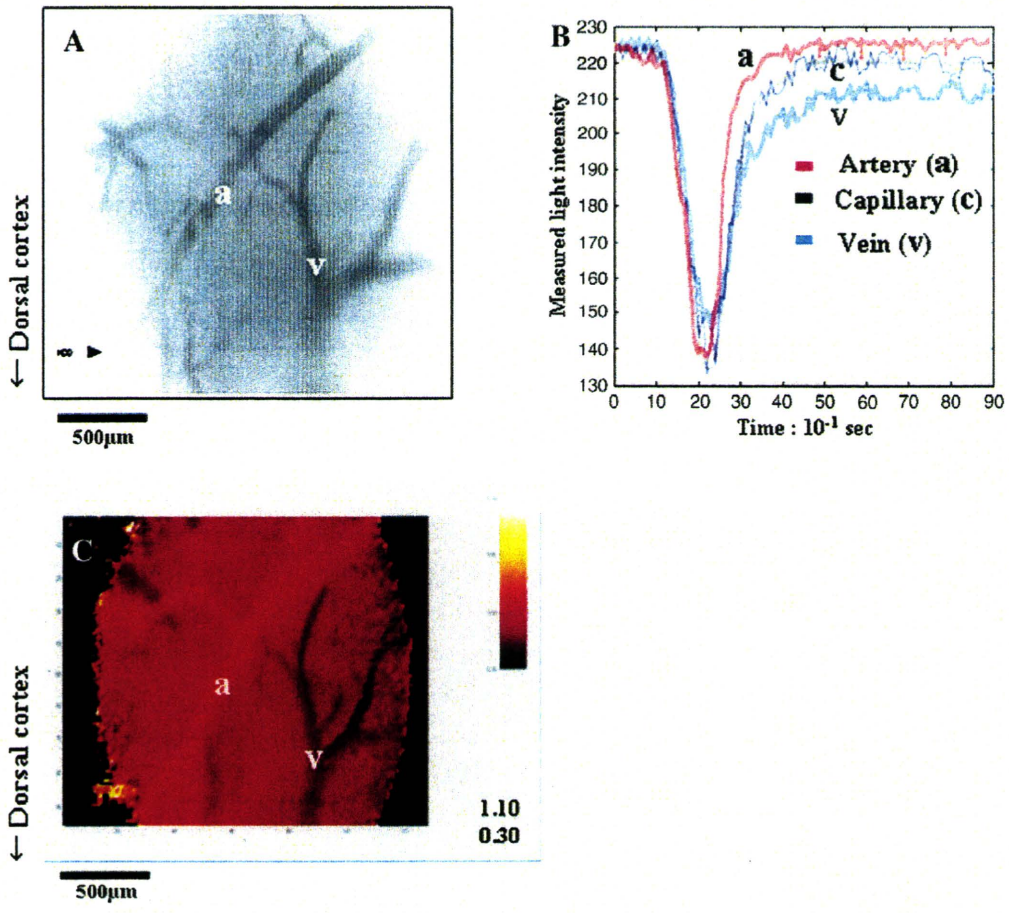

Fig. 1 – (A) Contrast-enhanced microphotograph of the mouse cerebral cortex taken from a video clip where a dye dilution process was recorded. A couple of vessels could be observed but their identification was difficult. (B) Dye dilution curves at a single selected pixel on an artery (red), a capillary (dark), and a vein (blue). The y-axis indicates the measured light intensity in arbitrary units, and the x-axis is the time in 10^{-1} s. (C) The 2-D microflow map, in which picture elements are pixelar 1/MTTs. This image can be compared with microphotograph A. The vessel appearing brown-yellow in color is definitely an arteriole, and those in dark colors are veins.

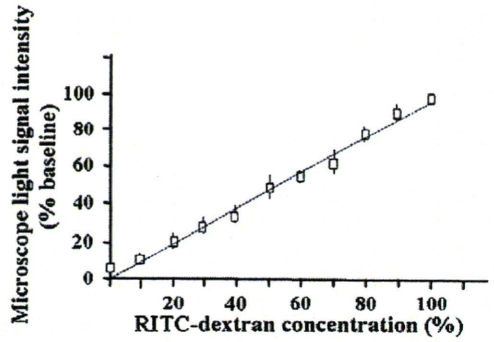

Fig. 2 – Graph showing the *in vitro* relationship between RITC-dextran concentration and the intensity of the light signal obtained by dynamic confocal microscopy.

Here, we describe the design and application of a method based on both the dye dilution principle and dynamic confocal imaging for semi-quantitative blood flow measurements with high spatial resolution in normal and ischemic mouse cortex. For recording of dye dilution curves in the mouse brain tissue, the dye was injected into the tail vein, since injection into the internal carotid artery may disturb cerebral circulation and is not appropriate for long-term observation. The use of intravenous injection is likely to have a smearing effect on the input function, but this was concluded to be sufficiently small for our purpose after appropriate comparisons (Fig. 1). The present optical imaging approach enabled us to obtain quantitative flow values repeatedly in the same ROI over several weeks. This method provides a powerful tool to investigate long-term changes of the cerebrocortical blood flow semi-quantitatively in the mouse and is expected to be particularly useful in view of the recent general trend to shift animal experiments from rats to mice.

2. Results

Physiological parameters were within normal limits, indicating that the mice were in good condition during the experimental procedures. Mean values were: MABP=105.8±10.8 mm Hg, PaO_2=101.1±17.4 mm Hg, $PaCO_2$=29.7±3.7 mm Hg, pH=7.42±0.04. Body weights of the mice did not vary significantly during the whole study.

2.1. *In vitro dye concentration*

There was a clear linear relationship between RITC-dextran concentration and the intensity of the light signal obtained by dynamic confocal microscopy (Fig. 2).

2.2. *Changes in blood flow caused by MCAo observed with LDF*

Upon coagulation of the MCA, a significant blood flow decrease was observed with LDF. The LDF value close to the occlusion site, which may correspond to the ischemic core (n=6), was significantly reduced to 25.9±9.3% of baseline within minutes (P<0.001). The LDF value in a more distal area that may correspond to the penumbra (n=6) was significantly reduced to a mean value of 45.6±9.6% of baseline (P<0.001). In sham-operated mice (n=5), no significant change in LDF occurred.

2.3. *In vivo dynamic confocal imaging*

The passage of RITC-dextran through microvessels just after injection into the tail vein, as well as during subsequent perfusion, was observed clearly by means of dynamic confocal microscopy (Fig. 3A, B). Arterial, tissue, and venous phases were visualized in subtraction pictures during the dye

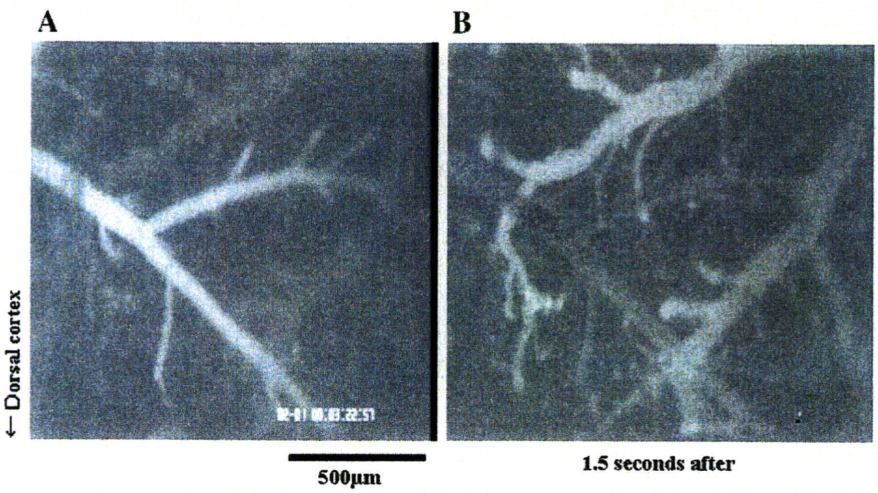

Fig. 3 – Typical example of the time course of the fluorescence signal after RITC-dextran intravenous injection video recorded through a dynamic confocal microscope. (A) Arterial phase of RITC-dextran passage through the microvessels in the mouse cerebral sensory cortex obtained by subtracting the first image of the brain surface (control video frame) from each subsequent experimental image. (B) Venous phase.

passage. The following parameters were calculated from these dynamic images.

2.3.1. 2-D flow maps

2.3.1.1. *Sham-operated mice.* Fig. 4A–D shows an example of 2-D flow maps and their histograms obtained in sham mice over 30 days. In these maps, bright yellow lines (fast flow) represent the terminal branches of the MCA. The calculated mean microflow values at day 0, at 10 min after MCAo, and at day 7 and day 30 were $0.52\pm0.06\ s^{-1}$, $0.52\pm0.04\ s^{-1}$, $0.53\pm0.04\ s^{-1}$, $0.54\pm0.05\ s^{-1}$, respectively. There were no statistically significant changes over time in the values of microflow of sham-operated mice.

2.3.1.2. *Ischemic mice.* Fig. 4E–H shows the obtained 2-D flow maps in the ROI of a typical MCA-occluded mouse. Under control conditions (Figs. 4E and 5A), the general color of maps was similar to that of sham-operated mice (Fig. 4A) with bright yellow lines delineating the MCA terminal branches. The mean microflow value under control conditions was $0.58\pm0.10\ s^{-1}$, which was not significantly different from

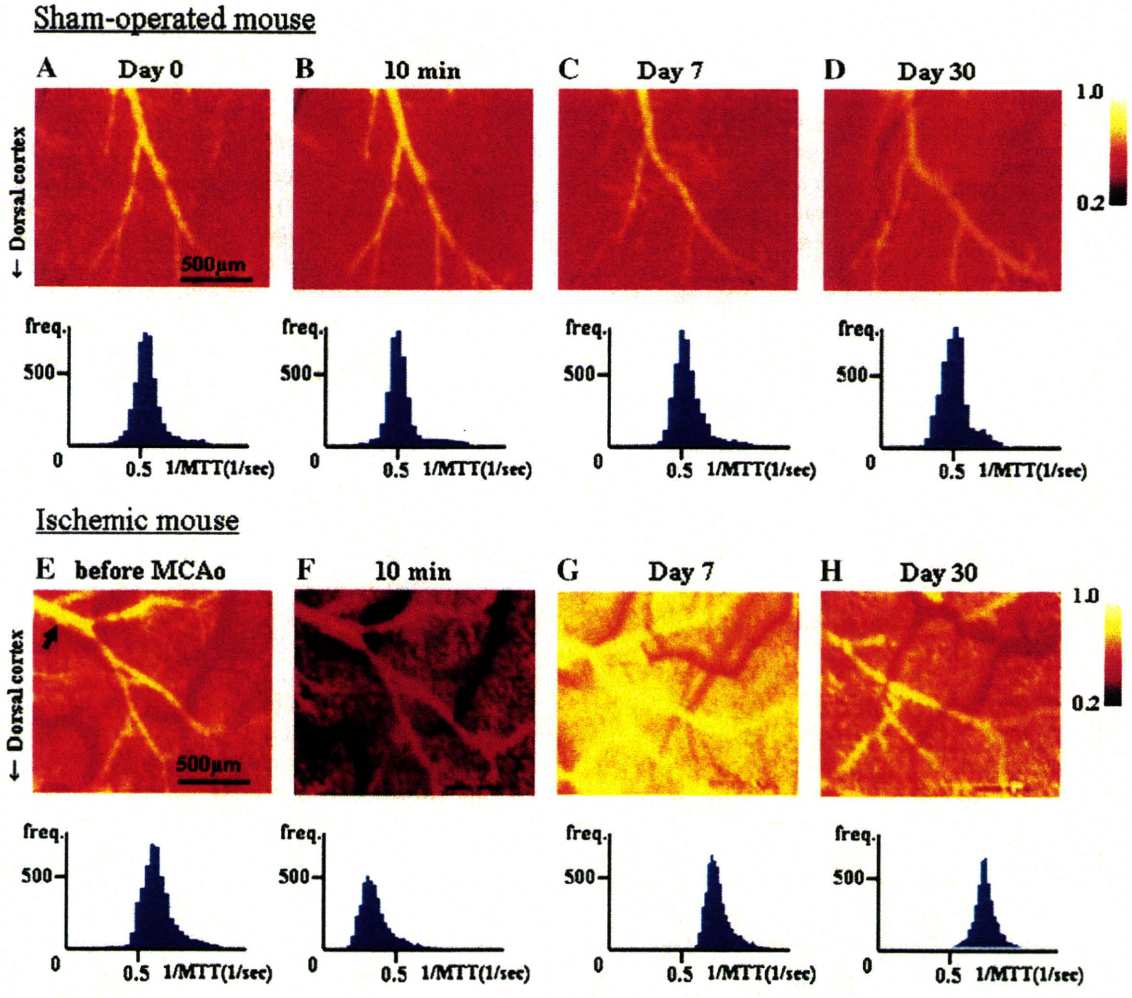

Fig. 4 – Time course of 2-D flow maps with a calibration scale in color representing graded microflow and their histograms. In 2-D flow maps, color reflects the reciprocal value of mean transit time of the blood flow. When the relative microflow increases, the color is brighter (towards yellow), while a decrease appears darker (towards black). Bright yellow lines (fast flow) represent arterioles, and black lines (slow flow) represent venules. In each histogram, the abscissa represents microflow velocity (s^{-1}) and the ordinate represents frequency. Upper panel: each graph corresponds to a time, day 0 (A), 10 min after (B), and 7 days after (C) and 30 days after (D), after sham operation. No statistically significant changes over time in microflow histograms occurred in any of the sham-operated mice. Lower panel: each graph corresponds to a time, day 0 (E), 10 min (F), 7 days (G) and 30 days (H), after MCAo. The arrow indicates the site of coagulation. Arterial occlusion produced an immediate decrease in the flow in downstream vessels. The histogram at 10 min after MCAo (F) moved to the left and the distribution became wider compared to that before MCAo (E). On day 7 (G), vascular velocities increased. The corresponding histogram shifted to the right. Some vascular remodeling could already be observed. On day 30 (H), the general color of the 2-D flow map and its histogram were similar to those under control conditions.

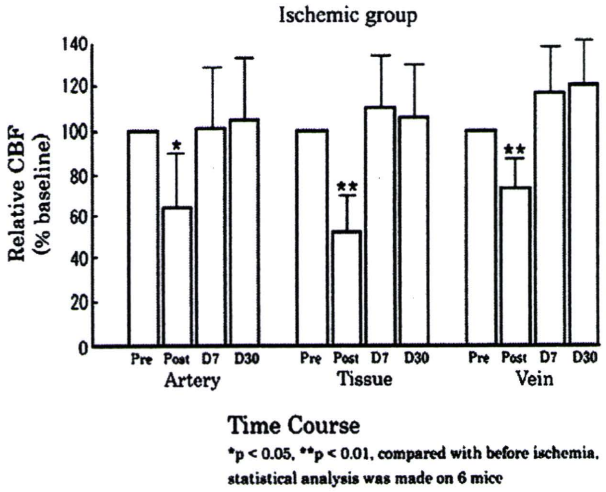

Fig. 5 – Time course of microflow changes of arterial, tissue, and venous components in ischemic mice, calculated separately using the "Zoom in" function of Matlab software ($n=6$). At 10 min after MCAo, there were statistically significant decreases in microflow of all components compared to control conditions. On days 7 and 30, these values had returned to those under control conditions. *$p<0.05$, **$p<0.01$ compared with before MCAo.

that of sham-operated mice ($P>0.05$). At 10 min after occlusion, the maps generally became darker, indicating a decrease in average flow velocities in the ROI (Fig. 4F), but the flow distribution was quite heterogeneous. At 7 days after MCAo, the maps had become yellow, showing the increase in average flow velocities in the ROI, probably owing to spontaneous reperfusion through the occluded artery (Fig. 4G). The mean microflow value was $0.64\pm0.05\ s^{-1}$, and the degree of reperfusion differed from mouse to mouse. At 30 days after occlusion, a marked remodeling of arterioles and venules was apparent in all mice. The subsequent time courses of 2-D flow maps were quite heterogeneous: in four cases, the general color in the 2-D flow maps was brighter than that under control conditions, while in other two cases, the color was darker than that under control conditions (Fig. 4H). Occasionally, even if blood flow had stopped completely at the occluded site, a clear bright yellow line in the lower part of the arteriole could be observed and the general color of the 2-D flow maps was brighter than that under control conditions. This finding indicates that blood flowed via collateral vessels, evidencing functional anastomoses.

2.3.2. *Histograms*

Histograms of blood flow of sham-operated and ischemic mice are also shown in Fig. 4A–H, respectively. In each histogram, the abscissa represents microflow velocity (s^{-1}) and the ordinate represents frequency. No significant changes of the positions or shapes of histograms occurred throughout the 30-day measurement period in any sham-operated mouse, with some minor, apparently spontaneous exceptions (Fig. 4A–D). In contrast, in each ischemic mouse, at 10 min after MCAo, histograms moved to the left and the distribution became wider than before MCAo, indicating a decrease of the average flow values in the ROI and an increase in their heterogeneity due to ischemia (Fig. 4F). At 7 days after MCAo, histograms were displaced to the right and the distribution was narrower than that obtained just after MCAo, suggesting some recovery of the average flow values and homogeneity (Fig. 4G). At 30 days after MCAo, the shape of histograms indicated a recovery to control conditions (Fig. 4H). The time courses of the changes in the histograms differed from mouse to mouse.

2.3.3. *Microflow changes of arterial, tissue, and venous components*

2.3.3.1. *Sham-operated mice.* There were no statistically significant changes over time in the values of microflow in arterioles, tissue, and venules of sham-operated mice.

2.3.3.2. *Ischemic mice.* The mean microflow values in the arteriole significantly decreased from $0.73\pm0.16\ s^{-1}$ to $0.47\pm0.19\ s^{-1}$ after MCAo ($p<0.05$). The mean microflow values in tissue and venules significantly decreased from $0.59\pm0.10\ s^{-1}$ to $0.33\pm0.07\ s^{-1}$ ($p<0.01$) and from $0.45\pm0.09\ s^{-1}$ to $0.32\pm0.06\ s^{-1}$ ($p<0.01$), respectively. At day 7 and day 30, the average mean blood flow values through arterioles, tissue, and venules returned to baseline and there were no statistically significant differences in comparison with the values of the pre-ischemic period. Percent changes are reported in Fig. 5.

2.3.4. *Moment analysis*

The results of moment analysis of microflows calculated from the histograms of ischemic mice are presented in Table 1. Just after arterial occlusion, both blood distribution (H) and mean microflow values were significantly decreased from 1.00 to 0.27 ($p<0.01$) and from $0.58\pm0.10\ s^{-1}$ to $0.44\pm0.08\ s^{-1}$ ($p<0.01$, arbitrary units), respectively. The decrease in H value upon arterial occlusion implies a decrease of blood amount distributed to the ischemic area. At 7 and 30 days after ischemia, blood distribution (H) was 114% and 75%, respectively, of that under control conditions (baseline). The mean values at these time points were $0.64\pm0.05\ s^{-1}$ and $0.63\pm0.07\ s^{-1}$, respectively. All these values at 7 and 30 days after MCAo were not significantly different from those under control conditions (baseline). The second moment (microflow heterogeneity γ) significantly increased from 0.45 ± 0.04 to 0.63 ± 0.12 ($p<0.01$) upon arterial occlusion. Subsequently, homogeneity was gradually restored.

In contrast, there were no statistically significant changes in the results of moment analysis in the sham-operated mice up to 30 days.

2.4. *Static confocal imaging*

2.4.1. *Sham-operated mice*

The whole superficial microvascular network was clearly observed from day 0 to day 30 after intravenous injection of RITC-dextran. The general microvascular architecture did not change throughout that period.

Table 1 – Results of microflows in the MCAo group.

		H/Hc	Mean	Variance	γ
Mouse 1	Before	1	0.67	0.08	0.42
	10 min	0.23	0.58	0.1	0.54
	Day 7	0.75	0.64	0.07	0.41
	Day 30	0.84	0.51	0.04	0.4
Mouse 2	Before	1	0.43	0.05	0.53
	10 min	0.18	0.39	0.09	0.78
	Day 7	1.02	0.63	0.06	0.4
	Day 30	1.33	0.64	0.04	0.33
Mouse 3	Before	1	0.58	0.06	0.43
	10 min	0.25	0.4	0.07	0.69
	Day 7	1.56	0.71	0.06	0.34
	Day 30	0.49	0.64	0.08	0.3
Mouse 4	Before	1	0.51	0.05	0.47
	10 min	0.36	0.36	0.03	0.54
	Day 7	1.21	0.66	0.07	0.41
	Day 30	0.7	0.65	0.07	0.42
Mouse 5	Before	1	0.68	0.08	0.41
	10 min	0.25	0.42	0.07	0.63
	Day 7	0.86	0.55	0.06	0.46
	Day 30	0.63	0.63	0.06	0.39
Mouse 6	Before	1	0.63	0.07	0.44
	10 min	0.37	0.5	0.08	0.58
	Day 7	1.47	0.63	0.05	0.36
	Day 30	0.56	0.72	0.07	0.38
Average (N=6)	Before	1	0.58	0.1	0.45
	10 min	0.27*	0.44*	0.08	0.63*
	Day 7	1.14	0.64	0.05	0.4
	Day 30	0.75	0.63	0.07	0.4

H=the height of rhodamine dilution curve; c=control.
Mean=the mean flow value in the ROI.
Variance=the dispersion of individual flow values in the 2-D flow map.
γ=the dimensionless dispersion (√Variance/Mean), which is an index of heterogeneity.
* $p<0.01$, compared with before ischemia, statistical analysis was made on 6 mice.

2.4.2. *Ischemic mice*

Under control conditions, the vascular network was similar to that of sham-operated mice. The terminal branches of the MCA could be clearly distinguished (Fig. 6A). One hour after MCAo, RITC-dextran leakage outside the vessels occurred, significantly reducing the image quality (Fig. 6B). Then we found that the recanalization took place within a few hours after ischemia by means of *in vivo* observation of the vascular condition through the cranial window with a surgical and confocal microscope.

On day 7 after MCAo, most of the vascular network was fluorescently labeled, and some vascular anatomical changes were observed (Fig. 6C). A weak fluorescence signal was still present in the tissue.

On day 30 after MCAo, no extravascular fluorescence was visible. A marked vascular remodeling of microvessel networks was present in all ischemic mice (Fig. 6D), as already described (Tomita et al., 2005b).

2.5. *Histology and immunohistochemistry*

2.5.1. *Sham-operated mice*

There was very little GFAP labeling at the edges of the window on day 30.

2.5.2. *Ischemic mice*

There was a small zone of necrotic tissue in the infarct epicenter, invaded by connective tissue. The boundary region of the lesion contained well-defined astrocytes with long processes on day 30 (Tomita et al., 2005b).

3. Discussion

In the present study, we describe a new approach, based on the 2-D flow map method (Schiszler et al., 2000) to semi-quantitatively and repeatedly measure local cortical "microflow" at the same ROI with high spatial resolution over a long period. The key feature of the method is that it permits repeated measurements of microflow changes and their correlation with time variable morphological changes of local microvasculature in exactly the same region after arterial occlusion for a period of more than 1 month.

The total quantity of RITC-dextran injected repeatedly into the tail vein to obtain the dye dilution curves in a mouse was

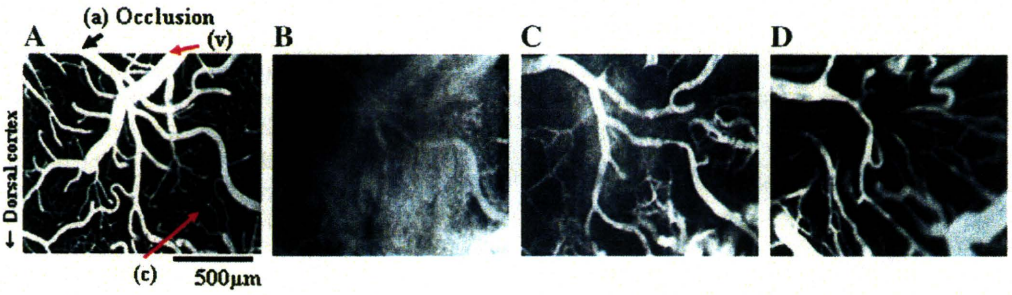

Fig. 6 – RITC-labeled microvessels visualized using a static confocal microscope. (A) Under control conditions. The whole microvascular network, including arterioles (a), venules (v), and capillaries (c) could be clearly distinguished. The black arrow indicates the site of occlusion. (B) One hour after MCAo. RITC-dextran leakage outside the vessels was observed. (C) On day 7 after MCAo. Vascular anatomical changes were observed. (D) On day 30 after MCAo. A marked vascular remodeling of microvessel networks was observed.

less than 60 mg/kg, which is far less than levels that would cause toxicity to the brain tissue (Rosenblum, 1978). Since the duration of each measurement was very short (<5 min), the laser illumination of the brain tissue also had no injurious effect.

As for the dye dilution technique, critiques might be raised about dispersion of the tracer injected into the tail vein; for example, if the bolus of RITC-dextran were sufficiently smeared during passage through the pulmonary circulation, mixing in the heart, and transport through the aorta and carotid arteries, the input function might be transformed to a shape very different from a spike. However, as shown in Fig. 3, the different phases, arterial, tissue and venous, could be clearly distinguished, implying that the dispersion was small enough to be negligible for the present purpose. As mentioned before, when a non-diffusible intravascular tracer is used, the flow changes depend largely on MTT, since MTT may vary many-fold from the control value to infinity, while cerebral blood volume (CBV) changes by only ±20% at maximum. For example, in the ischemic tissue induced by MCA occlusion in 31 cats, average CBV decreased from 6.3 vol.% to 5.5 vol.% (−13%), whereas 1/MTT decreased from 0.3/s to less than 0.1/s (more than −70%) (Tomita et al., 1980). It might be thought that CBV changes could be estimated from changes in the background brightness/darkness. However, Tomita M pointed out that such quantification of hemoglobin concentration in the tissue based on the Lambert–Beer law is infeasible because of the influence of the flow effect and other effects (Tomita et al., 2006; Tomita, 2006). The error introduced by the assumption that CBV remains unchanged can therefore be regarded as negligible (Tomita et al., 2002). In addition, we previously observed that the CBV did not change during an exsanguination–reinfusion procedure, using the same method (Schiszler et al., 2000). Theoretically, CBF values can be obtained as CBV/MTT. However, the range of CBV changes is from 6.3 vol.% to 5.0% in the gray matter, whereas MTT varies from 1 s to 10 s or more. Thus, we consider that reciprocal MTTs can be broadly regarded as representative of CBF values at a semi-quantitative level.

If we compare the present pre- and post-MCAo blood flow results in mice with those of a previously reported acute ischemic model in rats (Tomita et al., 2002), there is clear similarity: both flow and *H*, or the amount of blood volume redistributed to the pertinent ischemic area, decreased and the index of heterogeneity increased at the early phase after ischemia, and then these values returned gradually to basal levels. On the other hand, low-flow components in the histograms after ischemia were not prominent in the present study, presumably due to the milder degree of ischemia.

The use of the present technique in the post-ischemic state could help us to see the time course of collateral flow evolution and/or blood reperfusion (Toriumi et al., 2009). In four ischemic mice, at 7 days after MCAo, blood flow was significantly higher than that under control conditions ($p<0.05$). This indicates that spontaneous reperfusion after ischemia occurred, inducing hyperemia. Since we observed the microcirculation in the same region of the same mouse for at least 1 month, numerous destructive and repair processes would have contributed to the outcome. It is a unique feature of the present method that such processes as the appearance of collateral flow and reperfusion can be observed.

Coyle et al. measured cerebral blood flow based on the transport of microspheres through cerebral collateral vessels to the territory of the occluded MCA and to homologous tissue of the other hemisphere in Wistar–Kyoto rats (WKY) 1 month after MCAo (Coyle, 1987). The purpose of their study was to determine whether MCAo produces a sustained reduction in cerebral blood flow or whether collateral vessels restore blood flow to normal levels. They concluded that, at 1 month after MCAo, changes in the collateral vessels supplying the territory of the occluded MCA in WKY were sufficient to restore blood flow to normal under control conditions and to virtually normal levels during vasodilatation. Although the species of experimental animals and the method of inducing MCAo were different, our data on blood flow at 30 days after occlusion of the MCA are compatible with their conclusion.

Wei et al. (2001) tested the hypothesis that there are significant long-term local vascular changes after a ministroke that could form a basis for functional recovery. Based on the observation of changes at the brain surface after MCA ligation using FITC-transit through a cranial window, they concluded that arteriolar collateral growth and new capillaries support restored perfusion in the ischemic border after a ministroke and could support long-term functional recovery. As they suggested, the relationship between angiogenesis and/or vessel growth and function in the brain after focal ischemia has not yet been clearly characterized. The combination of our long-term *in vivo* investigation technique after focal ischemia with detailed histological examination might be a useful approach to this problem.

Our present long-term, semi-quantitative measurement technique has a spatial resolution ca. 500 times higher than that of the laser Doppler technique for measuring microvascular flow, and this makes it able to detect even small blood flow changes that might lead to very small ischemic lesions in the long term. If laser Doppler flowmetry had been employed, it would have been impossible to observe such a heterogeneous microflow decrease in a small ischemic area, since the flow would have been smeared, yielding only an average flow value lower than the control, and missing a critical value in the ischemic core. Ayata et al. (2004) showed that laser speckle flowmetry, which has advantages over laser Doppler flowmetry for CBF monitoring because of its high spatial resolution, could image the spatiotemporal dynamics of CBF changes after distal MCA occlusion in mice through an intact skull. While they demonstrated CBF changes in the acute phase after MCA occlusion, we could perform repeated *in vivo* analysis in the same ROI of the same mouse up to 1 month after distal MCA occlusion. Although our numerical moment analysis of the histogram of flow changes over a wide area may smear out heterogeneous changes, more detail could easily be obtained by focusing on flow changes in a specified small region. The idea of estimating flow velocity based on the contrast of laser speckle was initially proposed by Fercher and Briers (1981). The concept was to infer a temporal correlation time constant from the observed speckle contrast and subsequently to relate this time constant to the flow velocity. Many studies have reported a qualitative relationship, but as yet no convincing quantitative relationship has been proven, as noted by Duncan and Kirkpatrick (2008), who

have highlighted a number of issues that may prevent laser speckle contrast analysis from becoming a quantitative tool for the estimation of flow.

Wang et al. (2007) proposed that laser speckle contrast imaging (LSCI) is a promising, quantitative, minimally invasive method to achieve *in vivo* high-resolution (submillimeter) visualization of blood flow in exposed biological tissue. They used a thinned skull preparation, which they thought superior to full craniotomy. The intact dura mater allowed long-term investigation of the changes in the exposed cortical area within a single animal while preserving the integrity of the brain surface environment. However, they found that bone translucency changed during prolonged experiments. Therefore, several drops of mineral oil were applied to form a thin film in order to prevent drying and to improve the image quality. In comparison, our chronic window permitted long-term observation for at least 1 month after ischemia without special precautions.

The disadvantage of our technique is lack of temporal resolution. Although imaging can be repeated in longitudinal studies over long periods of time, our method is most useful to study rather static or slow-changing processes, and cannot be used to monitor perfusion changes that take place over seconds or even minutes, as can be done by laser Doppler or speckle flowmetry.

In conclusion, the present data show for the first time that semi-quantitative, repeated measurements of 2-D microflow can be performed in the long term at the same ROI in the same mouse with high spatial and temporal resolution, through a chronic cranial window, using *in vivo* confocal dynamic microscopy and intravenous tracer injection. Since accurate measurements of blood flow are still a matter of continuing investigation, such an approach represents a powerful tool to investigate long-term pathophysiological microcirculatory changes, or physiological microflow changes during various types of activation. The method described here should also be useful to determine the long-term effects of drug administration or gene deletion as approaches to protect damaged tissue and reduce the severity of infarction.

4. Experimental procedures

4.1. *Animal preparation*

Adult (12-week-old) male C57Bl/6J mice (Janvier Breeding Center, France) weighing 25.2±1.9 g were given free access to food and water and housed in a climate-controlled environment. All experimental procedures were carried out in accordance with international standards on animal welfare and were compliant with minimal standards as defined by the European Communities Council Directive of 24 November 1986. Experiments were performed under permit no. 02934 from the French Ministry of Agriculture. The methods of preparing the chronic cranial window and inducing focal ischemia were described in detail previously (Tomita et al., 2005b). Briefly, mice were anesthetized with 1.8–2.0% isoflurane and maintained with 1.4–1.6% isoflurane in a mixture of O_2 and N_2O delivered via a face mask. Rectal temperature was maintained at 37 °C using a retro-controlled homeothermic blanket (Harvard Apparatus, Holliston, MA, USA). The mouse was taken from animal care center when needed and was placed in a custom-built stereotaxic apparatus equipped for delivering anesthetic gas, fixing the head, positioning a laser Doppler probe, and stabilizing the ensemble under a confocal microscope. With this system, the mouse could be placed in the same position repeatedly for all investigations.

4.1.1. *Chronic cranial window*

All surgery was performed under an operating microscope (S21, Carl Zeiss, Oberkochen, Germany). A 3-mm-diameter hole was drilled above the left parieto-occipital cortex, 2.5 mm posterior to the bregma and 2.5 mm lateral to the midline (Franklin and Paxinos, 1997), keeping the dura intact. A circular 140-μm-thick quartz coverslip was fixed to the bone with dental cement (Ionosit, DMG, Hamburg, Germany), making the preparation waterproof. The area under the window corresponded to the distal territory of the MCA. Only mice whose cranial window was perfectly clear, without any bleeding or inflammatory process, were used for the study.

4.1.2. *Focal ischemia*

One week later, the mouse was placed in the same conditions as for cranial window implantation and an image of the whole vascular field was obtained via the surgical microscope (S21, Carl Zeiss, Oberkochen, Germany) using a digital camera (Coolpix 950, Nikon, Japan). Focal ischemia was then induced by topical thermocoagulation of two distal branches of the left MCA through the cranial window (Tomita et al., 2005b). To check the efficiency of arterial occlusion, changes in local blood flow at 2 sites over the window (one close to the MCA branch and the other distant from it) were recorded before and just after the occlusion, using a laser Doppler flowmeter (MBF 3D, Moor Instruments, Axminster, UK). Successful occlusion was also indicated by blanching of the underlying cortex.

4.2. *Measurements*

4.2.1. *Laser scanning confocal fluorescence microscopy.*

Mice were placed under the confocal microscope and maintained using the stereotaxic device under the same experimental conditions as for cranial window implantation and MCA occlusion (MCAo). Each mouse underwent a series of measurements just before sham operation ($n=5$) or arterial occlusion ($n=6$), i.e., under control conditions (day 0), 10 min after sham operation or MCA occlusion, and 1 week (day 7) and 1 month later (day 30). Each experiment took less than 1 h, and then the animal was returned to the animal center for routine care during the remaining time.

4.2.1.1. *Dynamic microscopy.* A Viewscan DVC-250 confocal laser scanning unit (BioRad, UK) attached to an Optiphot-2 fluorescence microscope (Nikon, Japan) was used to visualize the intravascular tracer. The light source was an argon/krypton laser whose wavelengths were 488, 568, and 647 nm. The objective was a Nikon dry lens (×4 or ×10). The numerical apertures were 0.40 and 0.55, and the working distances were 1.8 mm and 2.0 mm, respectively. The feature of this microscope is its linear pinhole, allowing real-time 2-D image acquisition. Appropriate filters were used.

For every flow measurement in each mouse, a tracer dose (<0.01 ml as a bolus) of Rhodamine B-isothiocyanate-dextran (RITC-dextran, molecular weight=71,200 Da; 20 mg/ml, Sigma, France) was injected via the tail vein to fluorescently label plasma and allow calculation of the regional mean transit time of blood (MTT). The tracer injection was repeated at 15-min intervals for a maximum of three times. The tail vein was occluded at the end of the experiment, and a new catheter was inserted slightly upstream for the next experiment, so that venous catheterization was performed at maximum of three times on each side.

A ROI was selected at ×10 magnification after the first RITC-dextran injection, but before starting the flow measurements. The location of the ROI could be easily recognized, using MCA branching as a landmark. The occlusion site was in the upper left quarter of the ROI, inducing blood flow arrest in downstream vessels. The size of the ROI was 1.3 mm×0.9 mm. The microscope was focused to reproducibly explore the ROI at the same brain depth, in the range of 100–200 μm.

Just after injection, RITC-dextran dilution images of microvessels in the pre-selected ROI at the surface of the cortex were recorded at video speed (25 frames per second) using an SIT camera (C-2400, Hamamatsu Photonics, Japan) and a digital video recorder (DSR-25 DVCAM, Sony, Japan) through the closed cranial window.

The images were stored on a PC using an 8-bit frame grabber card LG-3 (Scion Corp Inc, MA, USA) and processed using Scion Image software (Scion Corp Inc., USA) for repeated real-time data acquisition. Images of the same ROI in the same mouse were obtained three to four times in each experiment. Sequential frames of RITC-dextran dilution curves in the ROI over less than 5 s were analyzed with Matlab domain software (KEIO-IS1).

4.2.1.2. *Static microscopy.* After each sequence of dynamic acquisition of RITC-dextran dilution images, the mouse was placed under another confocal microscope to visualize the same vascular networks at higher definition. This static laser scanning confocal fluorescence microscope (MRC 600, BioRad, UK) was equipped with a classical pinhole, in contrast with the dynamic confocal microscope. The channel specific for Rhodamine was used. The summation of several planes made possible the visualization of a cortical volume up to 200 μm beneath the brain surface. The static images were used to help ensure reproducible location of the ROI for further blood flow analysis.

4.2.2. *Physiological parameters*

In a separate group of mice, an elongated polyethylene catheter (Biotrol, Paris, France) was inserted into the femoral artery ($n=6$) to monitor arterial blood pressure and to sample arterial blood for gas partial pressure analysis (PaO_2, $PaCO_2$) and pH (Ciba Corning Diagnostics Corp., Medfield, MA, USA) under strictly the same experimental conditions as for flow studies.

4.2.3. *Histology and immunohistochemistry*

The histologic procedures were performed at 1 month after the arterial occlusion ($n=5$ sham-operated and 6 ischemic mice). The mice used for the 1-month histologic study were those used for *in vivo* measurements.

Mice were deeply anesthetized with halothane and transcardially perfused with heparinized saline, followed by 4% paraformaldehyde in 0.1 M phosphate buffer at 4 °C, pH 7.4. Brains were removed, postfixed overnight in paraformaldehyde, and cryoprotected in 20% sucrose in phosphate buffer. Coronal sections (45 μm) were cut in a cryostat (CM3050S, Leica, Germany).

Every 10th section was stained with cresyl violet. Adjacent free-floating sections were incubated overnight at 4 °C with antibodies against neuronal nuclear antigen (NeuN, Chemicon, Temecula, CA, USA, 1/400), or glial fibrillary acidic protein (GFAP, Santa Cruz Biotechnology, CA, USA, 1/50). The reaction products were visualized using peroxidase avidin–biotin (Vectastain ABC Kit, Vector Lab, Burlingame, CA, USA) with diaminobenzidine as the substrate (DAB kit, Vector Lab). Specificity was checked on additional sections by omitting the primary antibody.

4.3. *2-D flow mapping method*

The details of the original 2-D flow mapping method have been reported elsewhere (Schiszler et al., 2000; Tomita et al., 2002). The density changes of the fluorescence signal were monitored during the passage of RITC-dextran in the 1.3 mm×0.9 mm ROI, by capturing 200 frames at a rate of 25 frames/s through an 8-bit frame grabber card (Scion LG-3), and the time sequence images obtained were stored in a PC. Differences were scaled to 8-bit images, i.e., 0 (brightest)–256 (darkest), with an intermediate level of 128, and displayed as pictures on the 256 gray scale, for which we employed arbitrary units of optical density (OD) for convenience. With the aid of Matlab domain software (KEIO-IS1), the ROI was divided into 50×50 matrices, creating 2500 dye dilution curves (OD(t), where OD indicates the optical density in a pixel at time t). The calculation was based on the conventional equations (blood distribution $H=\int OD\ (t)dt$ and mean transit time $MTT=\int t\cdot OD(t)dt/\int OD(t)dt$). The ratio of H was calculated as H/H_c where H is the blood distribution and c indicates the control. We tentatively defined 1/MTT as "microflow," which was displayed on a 2-D map and also plotted on the time variable as a frequency distribution (histogram). The microflow histogram was subjected to moment analysis using mathematical formulae which have been described previously (Tomita et al., 1983). With the help of Matlab software and our own software (KEIO-IS1), all MTTs in the matrix of 50×50 were calculated. In short, the first moment represents the mean microflow value (mean) in the ROI. The second moment represents the variance or dispersion of individual microflow values on the 2-D flow map. Since variance varies with mean, dimensionless dispersion (since curves were fitted to the gamma distribution, we termed the dispersion "γ") is a more practical measure, and was obtained as $\sqrt{}$variance/mean, resulting in an index of heterogeneity. The index of "γ" varied between zero (homogeneous or uniform flow throughout the ROI) and unity (an exponential distribution). In this study, the first and second moments for each of the 11 mice were obtained before, and at 10 min, 7 days and 30 days after MCA occlusion or sham operation, and compared. The microflow changes of arterial, tissue, and venous components were calculated separately using the "Zoom in" function of the Matlab software. The spatial

resolution of the method was 4 μm×4 μm for microphotographs and 40 μm×40 μm for 2-D flow maps.

Results are presented as means±SD. Statistical analysis was performed using the paired Student's t test.

4.4. *Theoretical and practical considerations on input function*

Unlike experiments in rats, in which dye was injected into the internal carotid artery (Schiszler et al., 2000), the present experiments in mice adopted dye injection into the tail vein as mentioned above. During its passage to reach the brain, the dye would be mixed with blood in the heart, as well as during its passage through the pulmonary circulatory system and arterial circulation. The input function of the dye would therefore be smeared, being distorted from the Dirac Delta function. This distortion, if large, would blur the vascular hierarchy of artery and vein in the brain tissue and cause underestimation of flow values. If dispersion in the input function is expressed as $c_{input}(t)$, where c is the concentration at time t and t is the time after dye appearance at the inlet of the cortical microvasculature, the dispersed dye is further dispersed in the tissue microvasculature owing to a dye dilution process in the cerebral arteries ($c_{artery}(t)$), capillaries ($c_{capillary}(t)$), and veins ($c_{vein}(t)$). However, the preceding function at each inlet ($c_{input}(t)$) has to be convoluted. The practical dilution curves at arteries (Ca(t)), capillaries (Cc(t)), and veins ((Cv(t)) will be given by

$$Ca(t) = c_{input}(t)^{*}c_{artery}(t)$$

$$Cc(t) = c_{input}(t)^{*}c_{artery}(t)^{*}c_{capillary}(t)$$

$$Cv(t) = c_{input}(t)^{*}c_{artery}(t)^{*}c_{capillary}(t)^{*}c_{vein}(t)$$

where * denotes a convolution integral.

KEIO-IS1 can calculate these functions at any given point on the microphotograph of the brain surface. This software analyzes a video clip of the dye dilution process, fractionates all dye dilution processes separately into matrices of 50×50 pixels, automatically calculates pixelar 1/MTTs (see below), and rearranges the calculated flow values to appropriate positions, thus yielding a microflow map. During these calculations with KEIO-IS1, it is easy to obtain individual dye dilution curves as Ca(t), Cc(t), and Cv(t) by placing the cursor on any target point (i.e., arteriole, capillary or vein) on the microphotograph and clicking the mouse (Fig. 1).

Microflow (CBF) in the tissue was calculated based on the Stewart-Hamilton principle

$$CBF_{tissue} = CBV_{tissue} / MTT_{tissue}.$$

As mentioned before, CBV_{tissue} was assumed to be constant during a procedure, since the CBV contribution to CBF changes was small compared with the MTT contribution. Therefore, no correction for CBV changes was made in the present study.

4.4.1. *Relationship between RITC-dextran concentration and intensity of the light signal obtained using dynamic confocal microscopy*

A concentration series of RITC-dextran from 0 to 100% (every 10%) was prepared and added to the wells of a culture plate (Falcon). The culture plate was placed under the dynamic confocal microscope described above. The light signal of each well was video recorded and stored in a PC through an 8 bit frame grabber card (Scion LG-3). The intensity of the light signal was calculated using Scion image software in the 256 gray scale.

Acknowledgments

This work was supported by grants from INSERM, CNRS, and University Paris 7. YT was funded by INSERM.

REFERENCES

Ayata, C., Dunn, A.K., Gursoy-Ozdemir, Y., Huang, Z., Boas, D.A., Moskowitz, M.A., 2004. Laser speckle flowmetry for the study of cerebrovascular physiology in normal and ischemic mouse cortex. J. Cereb. Blood Flow Metab. 24, 744–755.

Coyle, P.D., 1987. Blood flow through cerebral collateral vessels one month after middle cerebral artery occlusion. Stroke 18, 407–411.

Dirnagl, U., Villringer, A., Gebhardt, R., Haberl, R.L., Schmiedek, P., Einhaupl, K.M., 1991. Three-dimensional reconstruction of the rat brain cortical microcirculation *in vivo*. J. Cereb. Blood Flow Metab. 11, 353–360.

Duncan, D.D., Kirkpatrick, S.J., 2008. Can laser speckle flowmetry be made a quantitative tool? J. Opt. Soc. Am. A Opt. Image Sci. Vis. 25 (8), 2088–2094.

Fercher, A.R., Briers, J.D., 1981. Flow visualization by means of single-exposure speckle photography. Opt. Commun. 37, 326–330.

Franklin, K.B.J., Paxinos, G., 1997. The Mouse Brain in Stereotaxic Coordinates. Academic Press, San Diego.

Hudetz, A.G., Weigle, G.M., Fenoy, F.J., Roman, R.J., 1992. Use of fluorescently labeled erythrocytes and digital cross-correlation for the measurement of flow velocity in the cerebral microcirculation. Microvasc. Res. 43, 334–341.

Rosenblum, W.I., 1978. Fluorescence induced in platelet aggregates as a guide to luminal contours in the presence of platelet aggregation. Microvasc. Res. 15, 103–106.

Schiszler, I., Tomita, M., Fukuuchi, Y., Tanahashi, N., Inoue, K., 2000. New optical method for analyzing cortical blood flow heterogeneity in small animals: validation of the method. Am. J. Physiol. 279, H1291–H1298.

Seylaz, J., Charbonné, R., Nanri, K., von Euw, D., Borredon, J., Kacem, K., Meric, P., Pinard, E., 1999. Dynamic *in vivo* measurement of erythrocyte velocity and flow in capillaries and of microvessel diameter in the rat brain by confocal laser microscopy. J. Cereb. Blood Flow Metab. 19, 863–870.

Tomita, M., Gotoh, F., Sato, T., Amano, T., Tanahashi, N., Tanaka, K., Yamamoto, M., 1978. Photoelectric method for estimating hemodynamic changes in regional cerebral tissue. Am. J. Physiol. 235, H56–H63.

Tomita, M., Gotoh, F., Amano, T., Tanahashi, N., Tanaka, K., 1980. "Low perfusion hyperemia" following middle cerebral arterial occlusion in cats of different age groups. Stroke 11, 629–636.

Tomita, M., Gotoh, F., Amano, T., Tanahashi, N., Kobari, M., Shinohara, T., Mihara, B., 1983. Transfer function through regional cerebral cortex evaluated by a photoelectric method. Am. J. Physiol. 245, H385–H398.

Tomita, M., Schiszler, I., Tomita, Y., Tanahashi, N., Takeda, H., Osada, T., Suzuki, N., 2005a. Initial oligemia with capillary flow stop followed by hyperemia during K^+-induced cortical spreading depression in rats. J. Cereb. Blood Flow Metab. 25, 742–747.

Tomita, M., Ohtomo, M., Suzuki, N., 2006. Contribution of the flow effect caused by shear-dependent RBC aggregation to NIRS spectroscopic signals. Neuroimage 33, 1–10.

Tomita, M., 2006. Flow effect impacts NIRS, jeopardizing quantification of tissue hemoglobin. Neuroimage 33, 13–16.

Tomita, Y., Tomita, M., Schiszler, I., Amano, T., Tanahashi, N., Kobari, M., Takeda, H., Ohtomo, M., Fukuuchi, Y., 2002. Moment analysis of microflow histogram in focal ischemic lesion to evaluate microvascular derangement after small pial arterial occlusion in rats. J. Cereb. Blood Flow Metab. 22, 663–669.

Tomita, Y., Kubis, N., Calando, Y., Tran-Dinh, A., Méric, P., Seylaz, J., Pinard, E., 2005b. Long-term *in vivo* investigation of mouse cerebral microcirculation by fluorescence confocal microscopy in the area ofv focal ischemia. J. Cereb. Blood Flow Metab. 25, 858–867.

Toriumi, H., Tatarishvili, J., Tomita, M., Tomita, Y., Unekawa, M., Suzuki, N., 2009. Dually supplied t-junctions in arteriolo-arteriolar anastomosis in mice: key to local hemodynamic homeostasis in normal and ischemic states. Stroke 40, 3378–3383.

Wang, Z., Hughes, S., Dayasundara, S., Menon, R.S., 2007. Theoretical and experimental optimization of laser speckle contrast imaging for high specificity to brain microcirculation. J. Cereb. Blood Flow Metab. 27, 258–269.

Wei, L., Erinjeri, J.P., Rovainen, C.M., Woolsey, T.A., 2001. Collateral growth and angiogenesis around cortical stroke. Stroke 32, 2179–2184.

Microvascular Research 81 (2011) 97–102

Contents lists available at ScienceDirect

Microvascular Research

journal homepage: www.elsevier.com/locate/ymvre

Regular Article

Developmental and circulatory profile of the diploic veins

Haruki Toriumi *, Toshihiko Shimizu, Mamoru Shibata, Miyuki Unekawa, Yutaka Tomita, Minoru Tomita, Norihiro Suzuki

Department of Neurology, School of Medicine, Keio University, 35 Shinanomachi, Shinjuku-ku, Tokyo, 160-8582, Japan

ARTICLE INFO

Article history:
Accepted 9 November 2010
Available online 18 November 2010

Keywords:
Diploic veins
Development
RBC velocity

ABSTRACT

To examine the development of the diploic veins in the calvarium, FITC-dextran was injected into the tail vein. The total area of the diploic veins showed a continuous, age-dependent development. We also measured the red blood cell (RBC) velocities in the diploic veins using an *in vivo* imaging technique and revealed RBCs with a significantly high velocity and unidirectional characteristics at the entrance route. The route passed from the basal periosteum of the cranial bone via the dura mater and into the diploic veins. Our findings indicate the existence of communications between intra- and extra-cranial circulation.

Introduction

The diploic veins are located in the diploic space of the cranial bone. Although their existence was first reported more than 100 years ago (Langer, 1877), only a few studies have explored their anatomical or functional features. In 1921, Testut reported the continuous development of the diploic veins with age (Testut, 1921). In addition, a large individual variation in the bony encasement for the diploic veins has been reported, based on an autopsy study of cadavers (Zenker and Kubik, 1996) and radiographs of skull bone (Stenzel, 1954; Hershkovitz et al., 1999).

In terms of the role of the diploic veins, these vessels are thought to contribute to brain cooling because of reported communications between the meningeal and diploic veins (Kunz and Iliadis, 2007). This mechanism is assumed to play a crucial role in the maintenance of constant cerebral metabolism under pathological conditions, such as pyrexia, stroke or migraine.

During a trial observation of the cortical circulation of the brain through the thin transparent skull bone in mice, we incidentally observed that the diploic veins seemed to have communication with the intra-cranial circulation, and we considered that such communication, if present, would be important for understanding the intra-cranial circulation system. Therefore, we attempted to conduct a more extensive study on the age-dependent development of the diploic veins. In addition, to detect direct communications between the diploic veins and intra-cranial circulation in living animals, we measured the flow velocities in the diploic veins using a software application (KEIO-IS2) developed in our laboratory (Tomita et al., 2008).

Materials and methods

Animals

A total of 24 male C57BL/6J mice were used for the study (five 5-week-old mice with a body weight of 18–20 g, five 16-week-old mice with a body weight of 30–32 g, five 45-week-old mice with a body weight of 32–36 g for examination of the age-dependent development of diploic veins; six 12- to 16-week-old mice with a body weight of 22–25 g for the measurement of red blood cell (RBC) velocity; and three 12- to 16-week-old mice with a body weight of 22–25 g for the confocal study). The experimental procedures used in this study were approved by the Animal Welfare Committee of Keio University (No. 070083).

Preparation of skulls

The animals in each age group were anesthetized using inhalational isoflurane (1.6% in air, 480 ml/min) via a concentration-controllable anesthesia unit (U-400 Anesthesia Unit; Univentor Ltd., Zejtun, Malta) and then each mouse was fixed on a thermoregulated warm plate (BWT-100; Bioresearch Center Co., Ltd., Nagoya, Japan). The tail vein was catheterized for the injection of 0.4 ml of 0.25% fluorescein isothiocyanate (FITC)-dextran (mol wt., 70,000; Fluka, Stockholm, Sweden) to label the microvascular network. The FITC-dextran was clearly dissolved in the saline without filtration or centrifugation (Tomita et al., 2005). Since a preliminary experiment showed the completion of dye filling in the diploic veins at 90 s after the injection of FITC dextran, the animals were decapitated at 90 s after the injection of the dye. Then, the scalp was removed and the exposed calvarium was cut off with a pair of scissors in the horizontal plane along the orbito-foramen magnum line to open the cavity. The brain was enucleated

* Corresponding author. Fax: +81 3 3353 1272.
E-mail address: h.toriumi@a6.keio.jp (H. Toriumi).

0026-2862/$ – see front matter © 2010 Elsevier Inc. All rights reserved.
doi:10.1016/j.mvr.2010.11.004

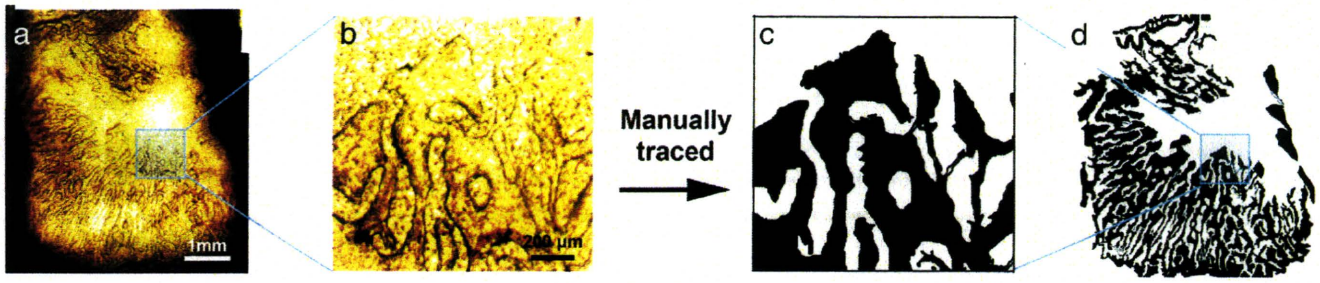

Fig. 1. (a) The silhouettes of the bone encasement of the diploic veins. (b) Enlarged image of (a). (c) Manual tracing of the image in (b), with the diploic veins depicted in black. (d) The manually traced image of (a) in its entirety. Scale bars; 1 mm for (a) and (d); 200 μm for (b) and (c).

from the skull cavity leaving the dura on the inner surface of the calvarium intact (Amaguri-method; Toriumi et al., 2007).

To observe the diploic veins with a microscope under fluorescence or transillumination, a small circle bank with 10 mm diameter was built on the slide with dental cement (Ionosit; DMG, Hamburg, Germany), and the bilateral parietal portion of the skull bones peeled off the dura mater were mounted on the slide with the inner surface of the calvarium upside.

For the observation under the confocal microscope to explore the relation between the dural vessels and the diploic veins, the dura mater of the skull bones was kept intact. The specimens were filled to the brim with saline and sealed with a cover glass. Confocal imaging was done on a Leica TCS-SP5 laser scanning microscope (Leica, Heidelburg, Germany) with a Kr/Ar laser fitted to a Leica DMI 6000 microscope running Leica confocal software (LAS AF v2.0). Serial confocal optical sections were taken through FITC-dextran that filled the parietal portion of the skull with the dura mater at 5 μm intervals for z-steps (10× objective). To create a movie file, files of z-series were converted to AVI flies by Leica confocal software.

Measurement of areas

The same specimens were used for the observation of the FITC-dextran-filled diploic veins and the bone encasement of the diploic veins. When we observed the whole skull, the developmental pattern of the diploic veins appeared homogenous in all parts of the skull. Therefore we chose the parietal portion of the skull, since it has a less curved surface and is most suitable for quantitative analysis.

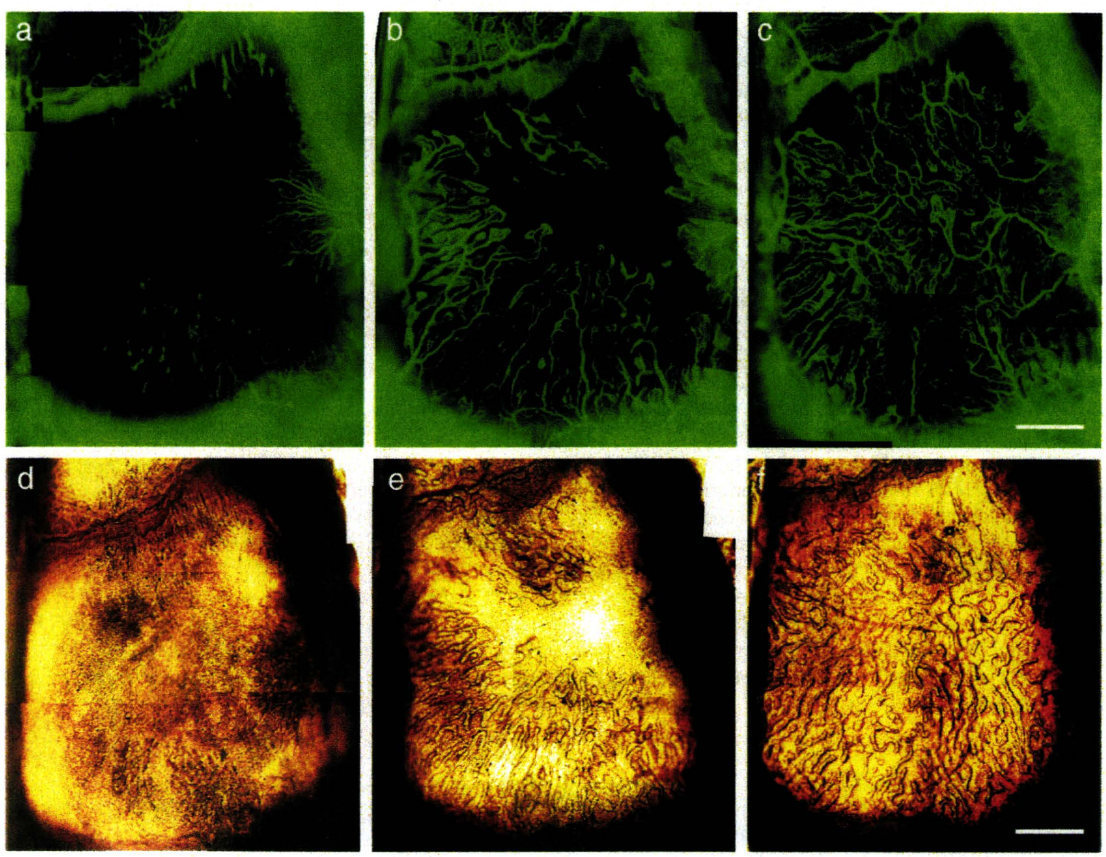

Fig. 2. Upper panel: Age-dependent development of the FITC-dextran-filled diploic veins at 5 weeks (a), 16 weeks (b) and 45 weeks (c). Lower panel: Age-dependent development of the bone encasement of the diploic veins at 5 weeks (d), 16 weeks (e) and 45 weeks (f) of age in the skull bone of the same mouse. Scale bars, 1 mm.

The FITC-dextran-filled diploic veins were visualized using fluorescence at an excitation wavelength of 488 nm, and the bone encasement of the diploic veins was observed under transillumination (Eclipse, TE 300; Nikon, Tokyo, Japan).

For quantification of the area of the FITC-dextran-filled diploic veins (Afdv), the green-fluorescent image of the FITC-filled diploic veins was framed so as to encompass the total observation area. The images were binarized into black (vascular) and white (background) pixels, which were scanned along the *y*-axis, and the black pixels (shadow of the vessels) were summed at the bottom. The summed black area thus obtained per total area was measured with the Image J analysis software (National Institutes of Health, Bethesda, MD). The measurement was made in all groups obtained from the 5-week-old, 16-week-old and 45-week-old mice.

For quantification of the Area of Bone encasement of the diploic veins (Abedv), the silhouettes of the bone cavities were taken as the TIFF images (Fig. 1a, b). Then, the edge of the bone cavity of the diploic veins was manually traced using Adobe Photoshop ver. 7.0, and the diploic veins were depicted in black (Fig. 1c, d). The images were binarized into black (vascular) and white (background) pixels, and the total area of the diploic veins of the parietal bone was measured as Abedv with the Image J analysis software. The measurement was made in all groups obtained from the 5-week-old, 16-week-old and 45-week-old mice.

Measurements of RBC velocity in the diploic veins

Male C57BL/6J mice aged 12–16 weeks were anesthetized using inhalational isoflurane (1.6% in air, 480 mL/min) via a concentration-controllable anesthesia unit (U-400; Univentor Ltd.). A tail vein was catheterized for intravenous injection of fluorescent materials. A 0.05 ml suspension of FITC-labeled RBC, which was prepared beforehand according to the method of Seylaz et al. (1999), was injected through the venous catheter. In some experiments, arterial blood pressure and heart rate were recorded by the intermittent cuff method using a cuff applied to the hindlimb and a non-invasive blood pressure monitor (MK-200; Muromachi Kikai Co., Ltd., Tokyo, Japan).

The surface of the parietal bone of each mouse was exposed, and fixed to a head-holder on the stage of the microscope. For measurements of RBC velocity, the high-speed camera laser scanning confocal fluorescence microscope and the image analyzing system were equipped with the following: an objective lens (LU Plan EPISLWD 20× NA = 0.35) or a water immersion lens (Plan Fluor 20× W NA = 0.50; Nikon, Tokyo, Japan), a multibeam confocal scanning unit (CSU22; Yokokawa, Tokyo, Japan), an image intensifier (C6653MOD-N; Hamamatsu Photonics, Hamamatsu, Japan), and a MotionPro high-speed camera (Motion Pro. Model 500) (Tomita et al., 2008). The MotionPro camera uses a digital imaging system with the MiDAS program (RED-Lake, San Diego, CA). Images of FITC-labeled RBCs of mice-parietal bone were acquired by excitation of an argon laser ($\lambda = 488$ nm; Melles Griot, Carlsbad, CA) at 250 frames/s (fps) for 10 s. These images were stored on a personal computer and processed in a MATLAB environment (The Math Works Inc., Natick, MA) using a software application (KEIO-IS2) developed in our laboratory. Details of the software were previously described (Tomita et al., 2008). Briefly, the images of the selected video clip were automatically analyzed for frame-by-frame movement of all RBCs to yield an RBC velocity map by frame-by-frame dislocation (distance) multiplied by the frame rate to yield a next frame, and by accumulation of RBCs to yield an RBC number map together with their color scales. All RBC velocity data with the identification numbers were then transferred to a spreadsheet (Microsoft Excel) for statistical analysis. For measurements of RBC velocity, we looked for the portion where the FITC-labeled RBCs were observed towards the diploic veins through the basal periosteum of the parietal portion of the cranial bone.

Statistical analysis

We used SPSS for Windows (version 15; SPSS Inc., Chicago, IL) for all statistical analyses. Differences between the groups were analyzed using an analysis of variance (ANOVA) followed by a post-hoc Tukey HSD for multiple comparisons.

Results

Age-dependent development of diploic veins

Fig. 2a, b, and c show the shape and structure (arborization) of FITC-dextran-filled diploic veins in mice of different ages. The FITC-dextran-filled diploic veins were relatively immature at 5 weeks, with only sprouting from the four corners (frontal, lateral, occipital, and medial sides) visible (Fig. 2a), and developed with age, as observed at 16 weeks (Fig. 2b). All the growing branches had connected to fill the empty space of the parietal area before the age of 45 weeks (Fig. 2c).

Transillumination of the skull vault silhouetted the vascular patterns corresponding to the FITC-dextran-filled diploic veins. However, the patterns were thicker, with a larger diameter, than the FITC-

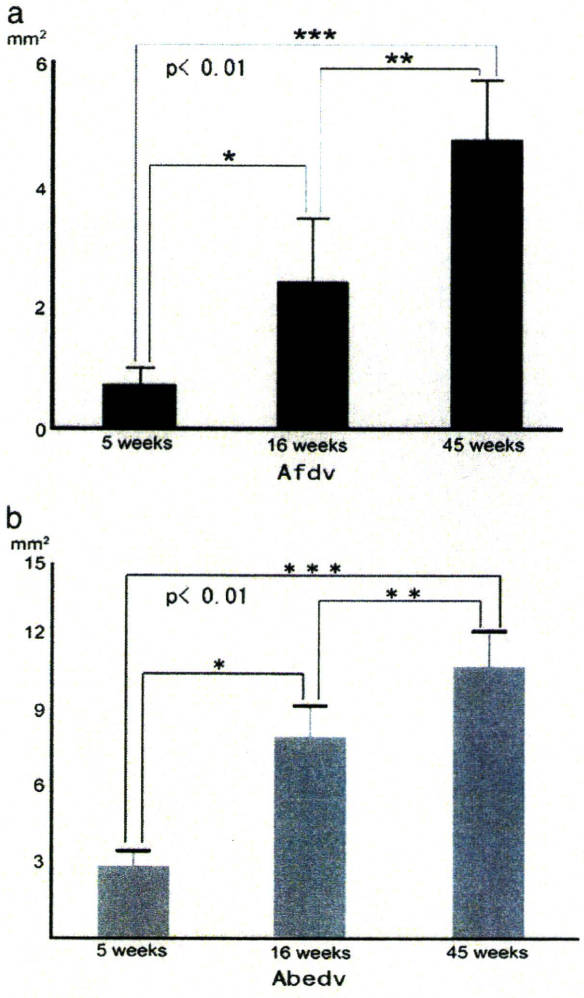

Fig. 3. (a) Afdv in the parietal bone. The bars represent age-dependent changes of the FITC-dextran-filled diploic veins. The area of the diploic veins was 0.73 ± 0.25 mm² (mean ± SD, $n = 5$) in 5-week-old animals, 2.43 ± 0.79 mm² ($n = 5$) in 16 weeks, and 4.75 ± 0.76 mm² ($n = 5$) in 45 weeks. (b) Abedv in the parietal bone. Abedv increased gradually from 5 weeks to 45 weeks. The areas were 2.7 ± 0.6 mm² ($n = 5$) at 5 weeks, 8.0 ± 1.4 mm² ($n = 5$) at 16 weeks, and 10.9 ± 1.2 mm² ($n = 5$) at 45 weeks of age. The differences among the different age groups in (a) and (b) were all statistically significant ($p < 0.01$).